



# Identification of small-molecule protein–protein interaction inhibitors for NKG2D

Aaron A. Thompson<sup>a,1</sup> , Michael B. Harbut<sup>b,1</sup>, Pei-Pei Kung<sup>a,1</sup> , Nathan K. Karpowich<sup>b</sup>, Jeffrey D. Branson<sup>b</sup>, Joanna C. Grant<sup>a</sup>, Deborah Hagan<sup>b,2</sup>, Heather A. Pascual<sup>a,3</sup>, Guoyun Bai<sup>a</sup>, Reza Beheshti Zavareh<sup>a,4</sup> , Heather R. Coate<sup>a</sup>, Bernard C. Collins<sup>a,5</sup>, Marjorie Côte<sup>a</sup>, Christine F. Gelin<sup>a</sup>, Kelly L. Damm-Ganamet<sup>a</sup> , Hadi Gholami<sup>a</sup>, Adam R. Huff<sup>b</sup>, Luis Limon<sup>a,6</sup>, Kevin J. Lumb<sup>b,7</sup>, Puiying A. Mak<sup>a,8</sup>, Kohki M. Nakafuku<sup>a</sup> , Edmund V. Price<sup>b</sup>, Amy Y. Shih<sup>a,8</sup>, Mandana Tootoonchi<sup>c</sup>, Nadeem A. Vellore<sup>a</sup> , Jocelyn Wang<sup>a</sup>, Na Wei<sup>a</sup>, Jeannie Ziff<sup>a</sup> , Scott B. Berger<sup>d</sup>, James P. Edwards<sup>a,9</sup>, Agnès Gardet<sup>c</sup> , Siquan Sun<sup>c</sup>, Jennifer E. Towne<sup>c</sup>, Jennifer D. Venable<sup>a</sup>, Zhicai Shi<sup>b</sup>, Hariharan Venkatesan<sup>a</sup>, Marie-Laure Rives<sup>a,10</sup>, Sujata Sharma<sup>b</sup>, Brock T. Shireman<sup>a,11</sup>, and Samantha J. Allen<sup>b,12</sup>

Edited by James Wells, University of California San Francisco, San Francisco, CA; received September 25, 2022; accepted March 10, 2023

**NKG2D (natural-killer group 2, member D) is a homodimeric transmembrane receptor that plays an important role in NK,  $\gamma\delta^+$ , and CD8<sup>+</sup> T cell-mediated immune responses to environmental stressors such as viral or bacterial infections and oxidative stress. However, aberrant NKG2D signaling has also been associated with chronic inflammatory and autoimmune diseases, and as such NKG2D is thought to be an attractive target for immune intervention. Here, we describe a comprehensive small-molecule hit identification strategy and two distinct series of protein–protein interaction inhibitors of NKG2D. Although the hits are chemically distinct, they share a unique allosteric mechanism of disrupting ligand binding by accessing a cryptic pocket and causing the two monomers of the NKG2D dimer to open apart and twist relative to one another. Leveraging a suite of biochemical and cell-based assays coupled with structure-based drug design, we established tractable structure–activity relationships with one of the chemical series and successfully improved both the potency and physicochemical properties. Together, we demonstrate that it is possible, albeit challenging, to disrupt the interaction between NKG2D and multiple protein ligands with a single molecule through allosteric modulation of the NKG2D receptor dimer/ligand interface.**

protein–protein interaction | inflammation | DNA-encoded library screening | NKG2D

Natural killer group 2D (NKG2D) is an activating type II transmembrane receptor encoded by the killer cell lectin-like receptor K1 gene. NKG2D is expressed as a homodimer on the surface of several types of lymphocytes including NK, NKT, CD8<sup>+</sup> T cells, and activated CD4<sup>+</sup> T cells, where it forms a complex with a homodimeric adapter protein known as hematopoietic cell signal transducer (HCST/DAP10) (1, 2). NKG2D recognizes at least eight ligands that are proteins related to major histocompatibility complex (MHC) molecules: MHC class I-related chain (MIC) A/B (MICA/MICB) and UL16 binding proteins (ULBP1–6) (3).

The expression of NKG2D ligands (NKG2DLs) is typically very low in healthy cells and increases in response to environmental stress, such as oxidative stress, DNA damage, and viral or bacterial infections (3). Ligand binding to NKG2D results in pro-inflammatory and cytolytic responses toward cells expressing NKG2D ligands, which constitutes a key immunosurveillance mechanism of cells compromised by malignancy or pathogen infection. In addition to its immunosurveillance role, NKG2D–NKG2DL signaling has also been implicated in chronic inflammatory and autoimmune diseases. The increased aberrant expression of NKG2DL in human disease tissues has been proposed to promote immune-mediated cell death/tissue destruction and exacerbation of inflammation in disease (4).

Given the complexity of NKG2D signaling, and its potential role in chronic inflammation, a small-molecule inhibitor of the protein–protein interaction (PPI) between NKG2D and NKG2DLs would be attractive to better understand and potentially intercept NKG2D biology. However, no such small-molecule inhibitors have been reported to date. This is not surprising as attenuating PPIs with a small molecule presents a high level of challenge for a drug discovery team, and in fact, only a small number of PPI inhibitors have been approved or progressed into clinical trials (5). One challenge is that many protein–protein interfaces encompass large amounts of buried surface area, with several discontinuous epitopes that are not immediately amenable to orthosteric disruption by small molecules (6). As revealed by several crystal structures of NKG2D bound to MICA, ULBP3, and ULBP6, NKG2D–NKG2DL interfaces are no exception, with total buried surface areas of approximately 2,000 Å<sup>2</sup> (7–9). Apo and ligand-bound structure

## Significance

The disruption of protein–protein interactions (PPI) represents a major opportunity for therapeutic intervention, as illustrated by many FDA-approved antibodies. However, the discovery of small-molecule PPI inhibitors remains challenging due to the complex nature and large size of most PPI interfaces. We report two distinct small-molecule classes targeting NKG2D (Natural killer group 2D), an immune receptor considered to be intractable for small-molecule inhibition. Inhibitor discovery and optimization were facilitated by large chemically diverse libraries combined with a comprehensive biochemical and cell-based assay suite. Both chemical series inhibited ligand-induced signaling by allosterically altering the NKG2D dimer conformation. This indicates that by targeting protein–protein interfaces involving oligomers, it is possible to increase the probability of discovering small-molecule PPI modulators.

<sup>8</sup>Present address: Computer-Aided Drug Design, Puiying Mak; Lead Finding Platform & Technology, Ferring Research Institute, San Diego, CA 92121.

<sup>9</sup>Present address: Samsara BioCapital, Palo Alto, CA 94301.

<sup>10</sup>Present address: Department of Biology, PostEra, Boston, MA 02110.

<sup>11</sup>Present address: Department of Chemistry, Rapport Therapeutics, San Diego, CA 92121.

<sup>12</sup>To whom correspondence may be addressed. Email: [sallen37@its.jnj.com](mailto:sallen37@its.jnj.com).

This article contains supporting information online at <https://www.pnas.org/lookup/suppl/doi:10.1073/pnas.2216342120/-/DCSupplemental>.

Published April 25, 2023.

comparisons show that while some ordering of disordered regions occurs upon complex formation, there are no significant conformational changes upon endogenous ligand binding to the dimeric interface. These observations are consistent with the proposal that NKG2D ligand binding degeneracy is achieved by “rigid adaptation” whereby a rigid binding site involving both monomers of the NKG2D homodimer makes diverse interactions with distinct endogenous ligands (10). This suggests that NKG2D does not undergo significant conformational changes upon binding to its various ligands and hence cryptic binding pockets may be difficult to predict.

In order to identify small-molecule inhibitors of NKG2D, we designed and implemented a comprehensive screening strategy that utilized a biochemical DNA-encoded library (DEL) screen and two cell-based high-throughput screens designed to identify molecules that interrupted the interaction between NKG2D and MICA. Using these complementary approaches, we screened over one billion molecules and identified two structurally distinct NKG2D inhibitors with low micromolar binding affinities. Surprisingly, despite their significantly different chemical structures, both hits bind to overlapping sites on the ligand-binding domain of NKG2D at the interface of the NKG2D dimer and display a unique allosteric mechanism of action. Through crystallographic analysis, we show that these small-molecule inhibitors captured a cryptic pocket that is likely formed by natural dynamics of the NKG2D dimer at the cell surface but is not observed in apo and NKG2DL-bound crystal structures and thus would be difficult to identify *a priori*. Upon binding at this allosteric interface, the small molecules hold the NKG2D dimer in an open conformation that affects the ability of NKG2D to engage MICA and other NKG2D ligands and initiate signaling. Finally, we demonstrated tractable SAR around one of the hit classes and the ability to obtain inhibitors with improved physicochemical properties and >10-fold increased potency from the original hit.

## Results

**Identification of Small-Molecule PPI Inhibitors of NKG2D.** Due to the inherent difficulty in identifying PPI-disrupting drug-like chemical matter, a comprehensive suite of assays was developed and deployed in multiple parallel screening campaigns against NKG2D to increase the probability of success (*SI Appendix, Fig. S1*). The first screen utilized a 1536-well ligand binding time-resolved fluorescence resonance energy transfer (TR-FRET) assay and was designed to identify compounds that directly block the interaction between NKG2D and MICA in a cellular context. The assay consisted of HEK293 cells stably expressing full-length SNAP-tagged NKG2D and DAP10, and a fluorescently labeled version of the extracellular domain (ECD) of MICA. We first validated this approach by demonstrating that extracellular MICA binds to full-length NKG2D with an apparent  $K_D$  of 200 nM (*SI Appendix, Fig. S2A*), consistent with  $K_D$ s of 103 nM and 48 nM determined using biochemical NKG2D/MICA time-resolved fluorescence resonance energy transfer (TR-FRET) and surface plasmon resonance (SPR) assays, respectively (*SI Appendix, Fig. S2 B and C*). Furthermore, this interaction was inhibited by untagged MICA and a control anti-NKG2D antibody 1D11 (*SI Appendix, Fig. S2 D and E*). Next, we screened over 500,000 small molecules from the Janssen internal screening library at a single concentration followed by dose–response experiments to confirm actives. A SNAP-tagged cellular GLP-1R/GLP1 TR-FRET counter-screen assay was used to remove technical artifacts and nonselective compounds, and a SNAP-tagged cellular

NKG2D/ULBP6 TR-FRET assay was developed to study the effects of inhibitors across NKG2D ligands. Finally, biochemical NKG2D/MICA TR-FRET, NKG2D, and MICA SPR binding assays, and cellular functional NKG2D-mediated cell-killing assays, were used for orthogonal confirmation (*SI Appendix, Figs. S1 and S2*).

The cellular NKG2D/MICA TR-FRET screening campaign identified one small-molecule hit (compound **1a**, Fig. 1A) from our internal compound screening deck with a cellular TR-FRET  $IC_{50}$  of 12.9  $\mu$ M (Fig. 1B). Compound **1a** also showed activity in a biochemical NKG2D/MICA assay ( $IC_{50}$  of 19  $\mu$ M) and bound to human NKG2D by SPR but not to human MICA or mouse NKG2D ( $K_D$  of 48.2  $\mu$ M, >80  $\mu$ M and >80  $\mu$ M for human NKG2D, human MICA, and mouse NKG2D, respectively) (Fig. 1C, D, and E and *SI Appendix, Fig. S3A*). Binding kinetics of **1a** to human NKG2D were slow relative to typical micromolar affinity molecules, with association ( $k_a$ ) and dissociation ( $k_d$ ) rates of  $7.64 \times 10^2 \text{ M}^{-1} \cdot \text{s}^{-1}$  and  $3.69 \times 10^{-2} \text{ s}^{-1}$ , respectively (Fig. 1D). To confirm the chemical structure and the initially assigned stereochemistry associated with this legacy file compound, we synthesized the four possible stereoisomers using stereospecific amino acid/ester starting materials (compounds **1a-d**, *SI Appendix, Table S1*). The activity of resynthesized **1a** was confirmed in the cellular NKG2D/MICA TR-FRET assay with an  $IC_{50}$  of 10.2  $\mu$ M (Fig. 1F). **1a** also showed partial inhibition ( $IC_{50}$  of 13.6  $\mu$ M) in the cellular NKG2D/ULBP6 TR-FRET assay, plateauing at an average of 58% inhibition across all replicates (Fig. 1F). The three alternate stereoisomers exhibited significantly weaker cellular TR-FRET activity relative to **1a** (*SI Appendix, Table S1*).

Notably, compound **1a** showed weak but measurable activity in a high-throughput cell-killing assay ( $IC_{50} \sim 40 \mu\text{M}$ , Fig. 1G). This coculture assay measured NKG2D-mediated cell killing of Ba/F3 cells expressing full-length MICA by the NK cell line KHYG-1, which endogenously expresses NKG2D. Alongside the ability to confirm functional inhibition by compounds identified in other screens, we reasoned that the presence of full-length receptor and full-length ligand may enable the identification of differentiated chemical matter, so we used this assay in a 1536-well format to screen 500,000 internal compounds. Ba/F3 lysis and CD20-based antibody-dependent cell cytotoxicity (ADCC) assays were used to filter out compounds that interfered with the assay readout or those that disrupted unrelated signaling pathways involved in immune cell activation downstream of NKG2D (*SI Appendix, Fig. S1*). Approximately 500 hits were obtained with  $IC_{50}$ s  $\leq 5 \mu\text{M}$  in the NKG2D cell-killing assay and no activity in the two counter-screen assays, but none of these compounds exhibited direct binding or inhibition in the biochemical or cellular NKG2D/MICA TR-FRET assays.

In a third approach to the identification of NKG2D receptor binders, we screened a one-billion-member DEL to find small-molecule inhibitors with potent binding affinity to the NKG2D protein. We designed the DEL screen selections to enrich for reproducible and potential functional binders by screening two forms of NKG2D (His-tagged and biotinylated) and by including a complex of NKG2D bound to its ligand MICA as a counter-screen. The DEL screen resulted in a series of related compounds with high enrichment factors when screened against NKG2D but not when screened against the NKG2D/MICA complex, suggesting that MICA prevented compounds from binding to the complex (**2a-d**, *SI Appendix, Table S2*). Compound **2a** displayed the strongest enrichment factors, and we synthesized a few analogs of this molecule as racemic mixtures by modifying the linking group which

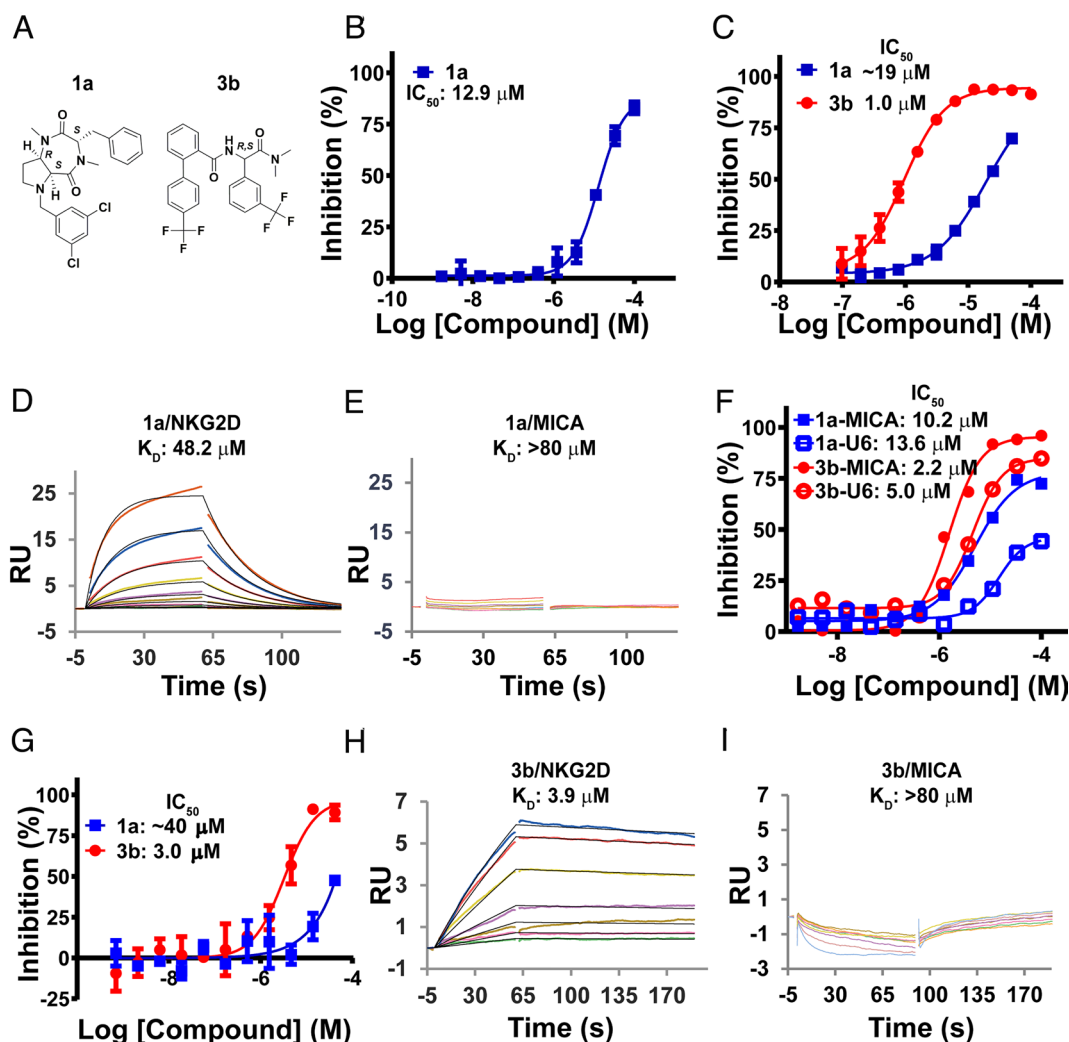


**Fig. 1.** Cellular, biochemical, and biophysical data for two NKG2D inhibitors identified from cellular HTS and DNA-encoded library screens. (A) Chemical structures of NKG2D inhibitors **1a** and **3b**. (B) Concentration-response curve of compound **1a** identified in the cellular TR-FRET NKG2D/MICA HTS campaign. (C) Representative concentration-response curves for compound **1a** (blue squares) and **3b** (red circles) in the NKG2D/MICA biochemical TR-FRET assay. (D) SPR sensorgram for compound **1a** binding to human NKG2D. Association ( $k_a$ ) and dissociation ( $k_d$ ) rates were  $7.64 \times 10^2 \text{ M}^{-1} \text{ s}^{-1}$  and  $3.69 \times 10^{-2} \text{ s}^{-1}$ , respectively. (E) SPR sensorgram for **1a** binding to human MICA. (F) Representative concentration-response curves for the inhibition of NKG2D binding to MICA (filled symbols) or ULBP6 (labeled as U6, open symbols) by resynthesized compound **1a** (blue squares) or compound **3b** (red circles) in the cellular NKG2D/MICA and NKG2D/ULBP6 TR-FRET assays. Mean  $IC_{50}$ s and SDs for **1a** in the cellular NKG2D/MICA and NKG2D/ULBP6 TR-FRET assays were  $10.2 \pm 2.9 \mu\text{M}$  and  $13.6 \pm 4.6 \mu\text{M}$ , respectively.  $IC_{50}$ s for **3b** are shown in Table 1. (G) Concentration-response curves for the inhibition of NKG2D-mediated cell killing of MICA-expressing cells by compound **1a** (blue squares) and **3b** (red circles) in the KHYG-1/Ba/F3 coculture assay. (H) SPR sensorgram for binding of compound **3b** to human NKG2D. Association ( $k_a$ ) and dissociation ( $k_d$ ) rates were  $1.44 \times 10^2 \text{ M}^{-1} \text{ s}^{-1}$  and  $5.67 \times 10^{-4} \text{ s}^{-1}$ , respectively. (I) SPR sensorgram for **3b** binding to human MICA. All error bars represent SDs from at least three independent replicates.

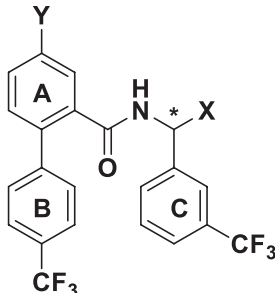
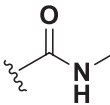
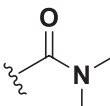
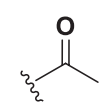
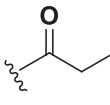
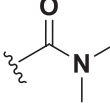
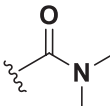
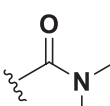
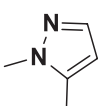
enabled attachment to the DNA (denoted by X, *SI Appendix, Table S2*). Accordingly, we synthesized the monomethyl amide (**3a**), dimethyl amide (**3b**), methyl ketone (**3c**), and ethyl ketone (**3d**) for this purpose (Table 1). Interestingly, dimethyl amide **3b** (Fig. 1A) displayed the highest potency among all the analogs synthesized in both cellular NKG2D/MICA and NKG2D/ULBP6 TR-FRET assays ( $IC_{50}$ : 2.2  $\mu\text{M}$  and 5.0  $\mu\text{M}$ ) (Fig. 1F), the biochemical NKG2D/MICA TR-FRET assay ( $IC_{50}$ : 1.0  $\mu\text{M}$ ) (Fig. 1C), and the NKG2D-mediated cell-killing assay ( $IC_{50}$ : 3.0  $\mu\text{M}$ ) (Fig. 1G). Specific binding of **3b** to NKG2D was also confirmed using SPR, with a  $K_D$  of 3.9  $\mu\text{M}$  for human NKG2D and >80  $\mu\text{M}$  for MICA and mouse NKG2D (Fig. 1H and I and *SI Appendix, Fig. S3B*). Similar to **1a**, binding kinetics of **3b** to human NKG2D were unusually slow relative to typical micromolar affinity molecules, with  $k_a$  and  $k_d$  values of  $1.44 \times 10^2 \text{ M}^{-1} \text{ s}^{-1}$  and  $5.67 \times 10^{-4} \text{ s}^{-1}$ , respectively). As mentioned previously, **3b** was prepared as a racemic mixture. Binding and inhibitory potency of the *S*-enantiomer were confirmed after we subsequently prepared the pure *S*-enantiomer of **3b**

(**3e**, Table 1). The corresponding *R*-enantiomer was found to be inactive at concentrations up to 20  $\mu\text{M}$  (**3f**, Table 1).

#### Inhibitor-Bound NKG2D Structures Identified a Cryptic Pocket.

To understand the binding mode and mechanism-of-action of compounds **1a** and **3e**, we obtained high-resolution crystal structures of both inhibitors bound to the ECD of NKG2D using cocrystallization (Fig. 2 and *SI Appendix, Table S3*). The asymmetric unit of all compound-bound structures presented here consisted of an NKG2D ECD homodimer. The 1.63-Å resolution cocrystal structure of **1a** revealed the compound positioned in an induced, cryptic pocket located in the middle of the NKG2D ECD, with the NKG2D homodimer splayed open by  $\sim 25^\circ$  compared with the homodimer of NKG2D bound to the endogenous agonist MICA (Fig. 2A, B, and D). With a volume of  $\sim 325 \text{ \AA}^3$ , as compared to  $\sim 70 \text{ \AA}^3$  in apo and MICA-bound structures (8, 11), the induced pocket extended into the hydrophobic interface and accommodated the entire molecule (Fig. 2A and B). The hydrophobic benzyl and

**Table 1. SAR of DNA-encoded library hits after off-DNA resynthesis**

						
Compound	*	X	Y	Cell NKG2D/MICA TR-FRET IC <sub>50</sub> ± SD (μM), LLE, (Max % Inh)	Cell NKG2D/ULBP6 TR-FRET IC <sub>50</sub> ± SD (μM), LLE, (Max % Inh)	NKG2D-mediated cell killing of MICA-expressing cells by KHYG-1 IC <sub>50</sub> ± SD (μM), (Max % Inh)
3a	<i>R,S</i>		H	7.4 ± 1.5, 1.7 (68)	>20, ND	~40, ND
3b	<i>R,S</i>		H	2.2 ± 0.7, 1.7 (97)	5.0 ± 0.9, 1.4 (86)	3.0 ± 1.1 (94)
3c	<i>R,S</i>		H	>20, ND	>20, ND	>40, ND
3d	<i>R,S</i>		H	3.0 ± 0.4, 1.5 (46)	>20, ND	>40, ND
3e	<i>S</i>		H	1.2 ± 0.6, 2.0 (101)	2.7 ± 1.1, 1.6 (98)	1.6 ± 0.4 (101)
3f	<i>R</i>		H	>20, ND	ND	>40
3g	<i>S</i>			0.3 ± 0.1, 2.9 (101)	0.7 ± 0.3, 2.6 (101)	0.4 ± 0.08 (105)

Mean IC<sub>50</sub> values and SDs were calculated from at least three independent experiments. Ligand-lipophilicity efficiency (LLE) was calculated based on calculated CHlogD. Maximum percent inhibition values (normalized to positive control of 100%) for active compounds are shown in parentheses.

dichlorobenzyl groups of **1a** protruded deep into a predominately hydrophobic cavity and the dichlorobenzyl moiety appeared to induce reorientation of Leu145 from one monomer for binding (Fig. 2B). Compound **1a** contains two carbonyl groups on the bicyclic core that participated in H-bond interactions with the backbone of Lys150 of both monomers at the surface of the homodimer (heavy atom distance of 2.88 Å, 134.8° to monomer A; 2.97 Å, 148.2° to monomer B), a region consisting of a mix of polar and hydrophobic atoms (SI Appendix, Fig. S4A). In available apo and NKG2DL-bound NKG2D structures, the backbone of residues Lys150 and Leu148 from each monomer made reciprocal H-bonding interactions with the opposite half of the homodimer (SI Appendix, Fig. S5A). Interestingly, the cocrystal structure with **1a** shows that these interactions are replaced by similar interactions

with the small molecule thereby acting as a wedge in the NKG2D ECD homodimer, driving the monomers apart (SI Appendix, Fig. S5B).

The 1.73-Å resolution structure of the DEL hit **3e** bound to NKG2D also showed the compound positioned at the homodimer interface of NKG2D ECD similar to the structure with compound **1a** (Fig. 2A and C). The resulting induced binding pocket exhibited a calculated volume of ~360 Å<sup>3</sup>, and again was made possible by compound-induced splaying of the homodimer by ~21° compared with the homodimer of MICA-bound NKG2D (Fig. 2A, C, and D). While the degree of splaying was similar in the **1a** and **3e** cocrystal structures, it should be noted that the wedging action of the inhibitors resulted in divergent rotations of the homodimer, presumably due to their different chemical structures and



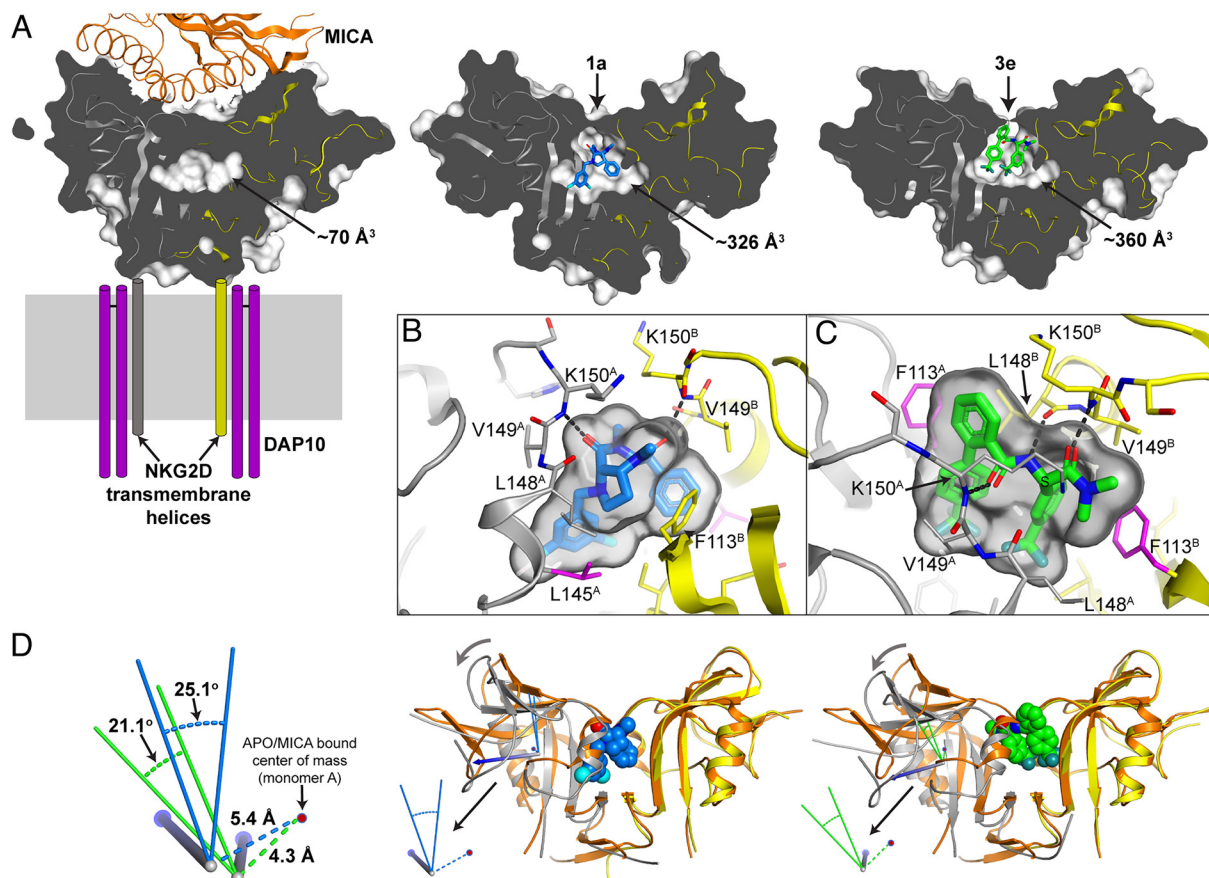


**Fig. 2.** Inhibitor-bound NKG2D structures revealed a cryptic pocket at the homodimer interface. Cross sections through NKG2D structures (monomer A and B colored gray and yellow, respectively) complexed with (A, Left) MICA (colored orange), (A, Middle) **1a** (colored blue), and (A, Right) **3e** (colored green). Close-up view of the induced pockets created by (B) **1a** and (C) **3e**. Residues that undergo conformational changes are colored magenta. Analysis of compound induced splaying of the NKG2D ECD; (D, Left) overlay of the displacement of the center of mass and the angle of rotation for monomer A of **1a** (blue) and **3e** (green) bound NKG2D compared with APO/MICA bound ECD after superpositioning onto monomer B. The rotation vector is represented with blue arrows. Structural overlays of monomer B from (D, Middle) **1a** and (D, Right) **3e** bound NKG2D with the MICA-bound NKG2D (PDB 1HYR; both NKG2D monomers colored orange; MICA not shown).

interactions with NKG2D (Fig. 2D and *SI Appendix*, Figs. S5C and S6).

The dual amide spine of **3e** participates in hydrogen bonding interactions with backbone residues at the surface of both NKG2D monomers (Fig. 2C and *SI Appendix*, Figs. S4B and S5C). The dimethyl amide of **3e** forms a single hydrogen bond to K150 of monomer B (heavy atom distance of 2.73 Å, 159.1° to K150<sup>B</sup>), and the secondary amide of **3e** forms hydrogen bond interactions with K150<sup>A</sup> and L148<sup>B</sup>, albeit with less-than-ideal angles (heavy atom distance of 3.0 Å, 109.3° to K150<sup>A</sup>; 2.97 Å, 144.9° to L148<sup>B</sup>). As described above for **1a**, intermolecular interactions between L148 and K150 were replaced by binding of **3e** to create a wedge in the homodimer. The two CF<sub>3</sub>-substituted phenyl groups (rings B & C) of **3e** protruded into the hydrophobic core of the nascent pocket and made numerous van der Waals interactions with the protein. Despite these contacts, the induced pocket contains unoccupied space proximal to the CF<sub>3</sub> groups that could be filled by additional substitution on the phenyl rings (Fig. 2C). **1a** and **3e** did not directly displace endogenous ligand binding but instead distorted the interface through which NKG2D interacted with its endogenous ligands. This interface distortion is consistent with NKG2D inhibition as observed in the cellular NKG2D/MICA TR-FRET, NKG2D/ULBP6 TR-FRET, and NKG2D-mediated cell-killing assays (Fig. 1 and Table 1).

Notably, both halves of the NKG2D homodimer of the **3e**-bound structure were structurally very similar to apo and

MICA-bound NKG2D structures, and all residue sidechains of the induced pocket were unaffected by compound binding and homodimer splaying except for Phe113 (Fig. 2C). Phe113 was observed in two different preferential orientations depending on the monomer; Phe113 from NKG2D monomer A (NKG2D<sup>A</sup>, monomer colored gray) was pointing up toward the NKG2DL interface and formed edge-face pi-stacking interactions with **3e**'s biaryl group (phenyl ring A & B). In contrast, Phe113 from monomer B (NKG2D<sup>B</sup>, monomer colored yellow) was pointing into the pocket where it was positioned under the dimethyl amide of the right hand side of the molecule (Fig. 2C).

**Optimization of DEL Hit 3e.** The two structurally distinct compounds from the cellular NKG2D/MICA TR-FRET (**1a**) and DEL (**3e**) screens displayed similar ligand efficiencies (LE) of 0.23 (LE =  $\Delta G$ /nonhydrogen atom count, ideal LE > 0.3) (12). However, **1a** displayed weaker activity in TR-FRET and cell-killing assays which directed us to focus our initial optimization efforts on **3e**. The optimization strategy for **3e** employed both parallel medicinal chemistry (PMC) as well as structure-guided design approaches. The phenyl ring A of **3e** was exposed to the interface between NKG2D receptor and its endogenous binding ligands (7–9). We therefore designed a PMC library to explore various substituents appended to ring A as well as various heteroaryl rings that replaced ring A to target this interface interaction. Among all analogs tested, the para-substituted *N*-methyl pyrazole-containing **3g** displayed a four-fold IC<sub>50</sub> improvement in

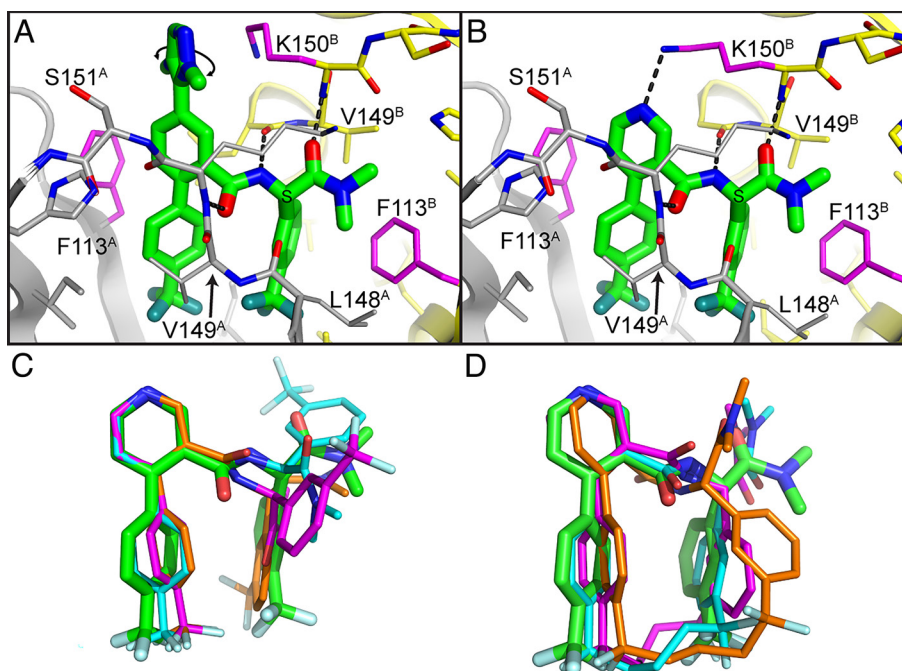


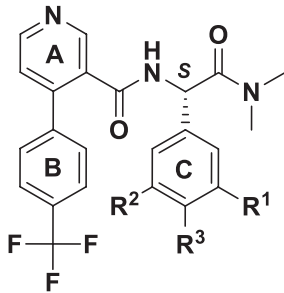
**Fig. 3.** Optimization of the DEL series. Close-up view of (A) **3g** and (B) **4a** bound at the homodimer interface of NKG2D. The methyl pyrazole of **3g** was fit with two alternative orientations as indicated with the double-headed arrow. NKG2D monomers A and B are colored gray and yellow, respectively, key residues are colored magenta and H-bonds are represented as black dashed lines. Conformers selected by NMR conformational analysis in dimethyl sulfoxide (DMSO) solution for (C) **4a** and (D) **4b** superposed on the X-ray structure conformer of **4a** (green).

cellular NKG2D/MICA TR-FRET and cell-killing assays relative to **3e** (Table 1). In addition, **3g** also demonstrated potent killing of MICA-expressing Ba/F3 cells by primary PBMCs ( $IC_{50}$ : 0.1  $\mu$ M) (*SI Appendix, Fig. S7A*) and showed an improved lipophilic ligand efficiency ( $LLE = pIC_{50} - cLogD$ , ideal  $LLE > 5$ ) (13, 14) value relative to **3e** (Table 1). Cellular TR-FRET assays confirmed the ability of **3g** to block the binding of multiple soluble recombinant ligands (human MICA, MICB, ULBP1, and ULBP6) to NKG2D with comparable  $IC_{50}$  values to one another (*SI Appendix, Fig. S7A*). In contrast, NK functional cell-killing assays showed differential

inhibition by **3e** depending on the NKG2DL present on the surface of Ba/F3 cells. While submicromolar inhibition of cell killing was observed for Ba/F3 cells expressing MICA, MICB, ULBP3, and ULBP5,  $IC_{50}$  values of  $>20$   $\mu$ M were observed for Ba/F3 cells expressing ULBP1, ULBP2, or two isoforms of ULBP6 (*SI Appendix, Fig. S7A*). This contrasted with the positive control anti-NKG2D monoclonal antibody 1D11 that showed consistent nanomolar inhibitory potency across all ligands tested.

The NKG2D/**3g**-bound structure suggested that the *N*-methyl pyrazole can adopt two alternate conformations, and the aliphatic

**Table 2. Optimization of DNA-encoded library hits**

Compound				Cell NKG2D/MICA TR-FRET $IC_{50} \pm SD$ ( $\mu$ M), LLE, (Max % Inh)	Cell NKG2D/ULBP6 TR-FRET $IC_{50} \pm SD$ ( $\mu$ M), LLE, (Max % Inh)	NKG2D-mediated cell killing of MICA-expressing cells by KHYG-1 $IC_{50} \pm SD$ ( $\mu$ M), (Max % Inh)
	R <sup>1</sup>	R <sup>2</sup>	R <sup>3</sup>			
4a	CF <sub>3</sub>	H	H	0.4 $\pm$ 0.1, 3.4 (100)	1.4 $\pm$ 0.2, 2.8 (102)	0.6 $\pm$ 0.2 (106)
4b	Macrocycle			1.4 $\pm$ 0.3, 2.9 (99)	4.5 $\pm$ 0.5, 2.4 (96)	1.6 $\pm$ 0.2 (100)
4c	CH <sub>3</sub>	H	H	0.7 $\pm$ 0.3, 3.2 (101)	0.9 $\pm$ 0.3, 3.1 (98)	0.4 $\pm$ 0.1 (102)
4d	CF <sub>3</sub>	CF <sub>3</sub>	H	0.2 $\pm$ 0.03, 3.1 (102)	0.5 $\pm$ 0.3, 2.8 (103)	0.2 $\pm$ 0.2 (103)
4e	CF <sub>3</sub>	CH <sub>3</sub>	H	0.1 $\pm$ 0.03, 3.5 (102)	0.4 $\pm$ 0.3, 2.9 (103)	0.2 $\pm$ 0.2 (107)
4f	CF <sub>3</sub>	Cl	H	0.1 $\pm$ 0.03, 3.4 (101)	0.2 $\pm$ 0.1, 3.1 (102)	0.2 $\pm$ 0.1 (105)

Mean  $IC_{50}$  values and SDs were calculated from at least three independent experiments. Ligand-lipophilicity efficiency (LLE) was calculated based on calculated  $cLogD$ .

sidechain of Lys150<sup>B</sup> was observed packing against this group in both orientations (Fig. 3A). It was unclear if the improvement in IC<sub>50</sub> for **3g** stemmed from a van der Waals interaction with Lys150<sup>B</sup> or from a steric interaction that would prevent binding of the endogenous ligands as the *N*-methyl pyrazole protruded out of the cryptic binding pocket and into the endogenous ligand binding site. However, removing the pyrazole and replacing the phenyl ring A of **3e** with a 4-pyridyl moiety (**4a**, Table 2) also improved potency relative to **3e** and LLE by more than 1 unit (LLE: 3.4 and 2.0, respectively). This suggests that any gains in potency are due to additional stabilization of the inhibitor-bound dimer which alters the binding site of the endogenous ligands, as opposed to a steric interaction that would directly prevent endogenous ligand binding. When comparing the potency and LLE values between **3g** and **4a**, **4a** displayed a better LLE value (3.4) relative to **3g** (2.9) although the two compounds displayed similar IC<sub>50</sub>s in the cellular assays (Table 2).

A cocrystal structure of **4a** was obtained (Fig. 3B) and was used for further ligand optimization via a structure-guided design strategy. The potency improvement observed for **4a** relative to **3e** may be due to hydrogen bonding interactions between the pyridyl moiety of **4a** and the sidechain of Lys150<sup>B</sup>, or it could be due to an increased edge-to-face interaction between the pyridyl moiety of **4a** with the side chain of Phe113<sup>A</sup> since this group is more electron withdrawing (15). Nevertheless, compound **4a** displayed similar potency to **3g**. These observations provided evidence that compound alterations within the cryptic binding pocket might be able to further improve the inhibitor potency.

Cocrystal structures revealed a hydrophobic channel between the two CF<sub>3</sub> groups of the compound B and C rings for several compounds, including **3g** and **4a** (Fig. 3). An NMR-based solution phase conformational analysis of **4a** further indicated that the lowest energy solution conformers of the molecule were different from the bound orientations observed in the cocrystal structure (Fig. 3C). Multiple possible conformers were identified in solution showing flexibility of the position of ring C where it could point up (cyan), sideways (purple), or down (orange) as in the bound conformation (green). This finding supported the design strategy to rigidify the solution conformation of the molecule in the bound orientation and to fill the lipophilic space mentioned above between the B and C rings through a macrocycle (**4b**, Table 2). However, the potency of **4b** was not improved relative to **4a**. A subsequent computational and NMR conformational analysis indicated that the macrocycle **4b** was still able to adopt multiple low-energy conformations (Fig. 3D) and unlikely to provide sufficient entropic gains to improve potency. Also of note, we replaced the *meta*-CF<sub>3</sub> group present in **4a** with a methyl moiety (**4c**), and this change resulted in similar potency and LLE (Table 2). Accordingly, we sought an alternate strategy to further optimize compounds and improve potency.

As a consequence of compound binding at the C2 symmetry axis of dimeric NKG2D, the electron density of these structures indicated the presence of two ligand orientations related by twofold rotation within the pocket (Fig. 4A and *SI Appendix*, Fig. S8). These observations highlighted an opportunity for filling the compound-induced pocket by symmetry-inspired hybrid design. Overlay of the symmetry-related **3e** molecules suggested that installation of CF<sub>3</sub> groups at both *meta* positions of ring C could more efficiently fill the hydrophobic pocket (Fig. 4A). This modification was well tolerated and resulted in slightly improved potency relative to the mono-CF<sub>3</sub> analog (compare **4d** with **4a**, Table 2). Introducing other *meta*-substituents, such as CH<sub>3</sub> and Cl in addition to maintaining the original *meta*-CF<sub>3</sub> substituent of ring C (**4e** and **4f**, respectively) further improved potency and LLE in both the MICA and ULBP6 assays (Table 2 and Fig. 4 B and C). While the bis-CF<sub>3</sub> of **3e** was tolerated, the cocrystal structures with **4e** and **4f** suggest that there is a preference for the larger CF<sub>3</sub> group pointing into monomer A (colored gray; Fig. 4C). Additionally, these structures suggested the importance of maintaining at least one hydrophobic group (at either R<sup>1</sup> or R<sup>2</sup>) in this pocket to anchor the binding of the phenyl ring C. This also helped us to understand the effects of the additional substituents at the alternate *meta*-position on ring C (R<sup>1</sup> or R<sup>2</sup>). In these cases, smaller substituents such as CH<sub>3</sub> or Cl pointed to a side pocket on NKG2D monomer A and did not appear to have a large effect on the positioning of ring C. A cocrystal structure of **4d** which contained the bis-CF<sub>3</sub> moiety showed a slight shift in the positioning of ring C suggesting that smaller *meta* groups could be preferred for ring C binding in a low energy state. Several unoccupied side pockets were observed in the vicinity of ring C, and optimization efforts directed toward these pockets will be discussed in an upcoming manuscript.

## Discussion

NKG2D activation has been proposed to play a role in the inflammation and tissue damage of multiple immune-mediated diseases (4). It is hypothesized that preventing NKG2D from interacting with its ligands would block cytolytic activity toward ligand-expressing cells and potentially restore tissue health and dampen inflammation. Antibodies are usually the first modalities explored for therapeutic PPI inhibition due to the difficulty in discovering small molecules with high affinity toward the generally large and flat space of PPI interfaces. Indeed, this was the case for NKG2D, as pockets at either the dimer interface or ligand binding region were observed to be shallow and likely challenging for specific binding of small molecules.

The use of three orthogonal screening strategies and a comprehensive assay suite enabled us to identify two structurally distinct, bona fide NKG2D binders/inhibitors. These NKG2D

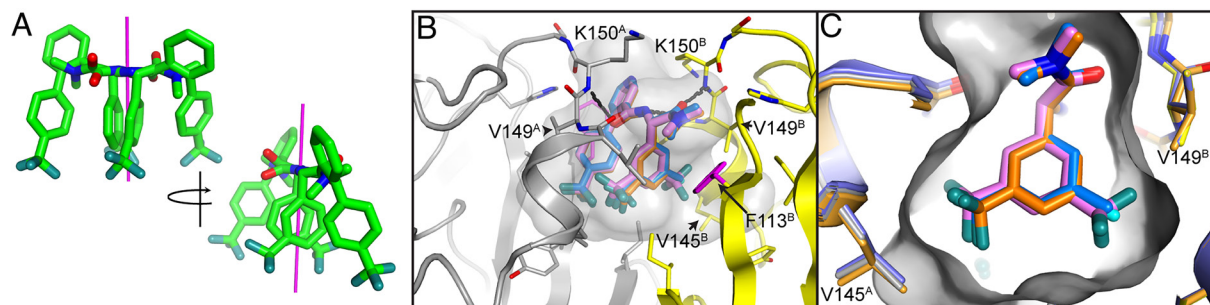


**Fig. 4.** Symmetry inspired optimization of DEL series. (A) Two molecules of **3e** related by a twofold symmetry axis at the center of the NKG2D homodimer as observed in the electron density maps (*SI Appendix*, Fig. S8). (B) Overlay of **4d** (colored violet), **4e** (colored blue), and **4f** (colored orange) in the cryptic pocket depicted with a surface representation (calculated by Hollow). (C) Close-up view of the overlay from panel B.



small-molecule inhibitors have a unique allosteric mechanism of action which differs from that of known antibody-based NKG2D-PPI disruptors. Small-molecule inhibitors with micromolar affinity typically display fast binding kinetics, but both chemical series of NKG2D inhibitors showed unusually slow association and dissociation rates in SPR (Fig. 1 *D* and *H*). This was particularly true for the association rate, which was remarkably similar between two hits and a little faster for the HTS hit ( $7.64 \times 10^2 \text{ M}^{-1} \text{ s}^{-1}$ ) than the DEL hit ( $1.44 \times 10^2 \text{ M}^{-1} \text{ s}^{-1}$ ) even though the DEL hit was over 10-fold more potent. We hypothesized that slow binding kinetics may be due to a conformational change between the unbound and inhibitor-bound forms of NKG2D, and indeed, high-resolution cocrystal structures of NKG2D provided insights into a unique inhibition mechanism. Notably, both of the chemically distinct series of inhibitors bound to a cryptic pocket at the NKG2D dimer interface and acted as a wedge to drive the monomers apart, thus altering the dimer in a way that disrupted ligand binding. These inhibitors are relatively small (<550 Da), and their size appeared to be advantageous for this mechanism, presumably because it enabled the inhibitors to fit between the two NKG2D monomers and alter the orientation of one monomer related to the other. In the case of the DEL screen where single pharmacophore and dual pharmacophore libraries of different molecular weights were screened side-by-side, the higher molecular weight libraries did not appear to provide additional chemical matter relative to the lower molecular weight libraries, at least for NKG2D (16).

Analysis of apo and endogenous ligand-bound structures reveals a small void located in the middle of the homodimer interface containing a volume of  $\sim 70 \text{ \AA}^3$  (PDB 1HYR used for analysis), but the cavity lacks an obvious access channel for engagement by small-molecule inhibitors. However, binding of **1a** and **3e** causes an increase in the size of the cryptic binding pocket by approximately fivefold to  $325 \text{ \AA}^3$  and  $363 \text{ \AA}^3$ , respectively. The mechanism by which inhibitors gain access remains unclear, although we hypothesize that they may take advantage of natural dynamics of the protein dimer. While a small, buried void is present at the dimer interface in apo and NKG2DL-bound structures, it would be nearly impossible to predict this pocket as a ligandable binding site with standard computational approaches. Despite inducing a pocket with a smaller volume, **1a** splays the ECD to a larger degree and causes a larger displacement in the center of mass compared to **3e** (Fig. 2*D*). The larger angle and displacement values did not result in higher potency for **1a**, so it is possible that other changes in the ECD quaternary structure and binding affinity better correlate with  $\text{IC}_{50}$  values.

It has been well documented that a single binding interface comprised of equivalent NKG2D monomers can interact with distinct surfaces of divergent monomeric ligands (9–11, 17, 18). Structures of NKG2D ECD in complex with diverse endogenous ligands suggest that this degenerate binding (binding of multiple, diverse ligands) is achieved through rigid shape-complementarity and a balanced combination of electrostatic and hydrophobic interactions with the dimeric binding surface of the ECD in a process that has been termed “rigid adaptation” (10). Under this mechanism, conserved patches on both halves of the rigid homodimer binding surface of NKG2D make assorted interactions with individual ligands. This rigid mechanism for achieving ligand degeneracy is a departure from the induced fit mechanisms that are widely utilized by many immunological receptor–ligand interactions including antibodies and TCR–peptide MHC class I complexes (19–22).

The concept of rigid adaptation could partially explain compound potency differences observed depending upon the

endogenous ligand used in cellular TR-FRET and NKG2D-mediated cell-killing assays. Weak inhibitors such as compounds **1a**, **3a**, and **3d** behaved differently with respect to potency and maximal inhibition values in the MICA and ULBP6 TR-FRET assays, with compound **1a** plateauing at 80% inhibition for MICA, and 58% inhibition for ULBP6 (Fig. 1*F* and Table 1). Compounds **3a** and **3d** were even more pronounced, as these inhibitors exhibited single-digit micromolar  $\text{IC}_{50}$ s and submaximal inhibition of MICA binding (68% and 46%, respectively) in the MICA TR-FRET assay but showed >20  $\mu\text{M}$  inhibition in ULBP6 TR-FRET and cell-killing assays (Table 1). This is consistent with these compounds acting as potential mixed inhibitors that bind to NKG2D but do not elicit a sufficiently large conformational change to fully inhibit binding of one or more of the endogenous ligands. As the TR-FRET assays were run at the  $K_D$  of the endogenous ligand, these discrepancies do not appear to be solely due to a different fraction of ligand bound to NKG2D.

While more potent compounds such as **3g** did not show differences in potency or maximal inhibition in the MICA and ULBP6 TR-FRET assays using soluble NKG2D ligands (Table 1), compound **3g** exhibited ligand-dependent inhibition when tested in a series of NKG2D-mediated cell coculture killing assays. **3g** consistently inhibited NKG2D-mediated killing of cells expressing MICA, MICB, ULBP3, and ULBP5 with submicromolar potencies (*SI Appendix*, Fig. S7*A*). However, **3g** showed minimal activity in cell-killing assays against ULBP1, ULBP2, and ULBP6. This was not unique to compound **3g**, as similar behavior was observed across the series. In comparison, a tool antibody inhibitor (1D11) showed equipotent inhibition for all NKG2D ligands. Ligand-dependent inhibition was consistent across different target/effector cell ratios, suggesting that the differences we observe are not likely due to ligand expression level. It is possible that NKG2D/NKG2DL affinities play a role in ligand dependence. While the affinities we measured between NKG2D and soluble ligands do not fully support this, we cannot definitively rule it out as affinity information for full-length cell surface ligands is not available. Ligand-dependent inhibition may also be due to differences in residues comprising the NKG2D/NKG2DL interfaces that make the inhibitors less effective at fully preventing NKG2D-mediated signaling for some ligands, even at full inhibitor occupancy. Indeed, previous reports indicate a considerable degree of sequence dissimilarity between the NKG2D/NKG2DL interfaces with an overall pairwise sequence identity of ligands of only 23 to 27% (11). Furthermore, the residue pairs at the PPI surface are quite variable as each ligand forms a diverse set of interactions consisting of hydrogen bonds, hydrophobic contacts, and salt bridges, although some overlap is observed (*SI Appendix*, Fig. S7 *B* and *C*) (7–9). Despite these significant ligand-dependent differences, the common requirement for the NKG2D dimer at the interface suggests that it may be possible to improve cross-ligand compound potency by twisting and wedging the NKG2D monomers further apart from each other.

As described above and in contrast to the lack of efficacy against ULBP1 and ULBP6 in cell-killing assays, **3g** inhibited the binding of recombinant soluble ULBP1 and ULBP6 to cellular NKG2D with similar potency to that observed for MICA (*SI Appendix*, Fig. S7). The reason for this discrepancy is not known but may be due to the inability of soluble ligands to fully recapitulate the effect of local concentration and presentation of the NKG2D ligands on the cell surface. In any case, this highlights the complex challenge of discovering and optimizing NKG2D small-molecule inhibitors with cross-ligand potency as it suggests that NKG2D/NKG2L interactions are variable in nature and may be affected by the ligand form (soluble vs. membrane-bound). This also underscores the



critical need for a detailed understanding of biology to identify the most relevant ligands for a given disease, as well as a comprehensive in vitro assay suite containing multiple NKG2DLs to enable the discovery of functional and cross-ligand NKG2D inhibitors.

While we were expecting to discover PPI inhibitors that sterically blocked binding at the receptor–ligand interface, using parallel screening approaches we converged on two distinct allosteric small-molecule PPI inhibitors. Both compounds function by distorting the quaternary conformation of the NKG2D ECD, thus reducing the ability of this receptor to respond to ligands. The combination of structural and assay data informed tractable SAR for this class of unique protein–protein inhibitors. Our medicinal chemistry design strategy improved cellular TR-FRET potency over 10-fold and improved ligand lipophilic efficiency (LLE) by more than 1 unit compared with the original DEL screening hit. Although the initial strategy of rigidifying the bound inhibitor conformation did not yield potency improvements, filling the binding pocket while maintaining flexible molecular conformations afforded more fruitful results. This study resulted in three key lessons. First, cryptic pockets present new and unexpected opportunities to identify allosteric small-molecule PPI inhibitors. Our inhibitors accessed a cryptic pocket that is reminiscent of previous studies such as IL-2 for which a small-molecule inhibitor Ro 26-4550 bound to and stabilized a cryptic site in IL-2 that was not observed in the apo protein (6, 23). Second, by targeting receptors that require oligomerization for ligand binding, it is possible to inhibit PPIs without the requirement for a natural pocket within the monomer. Targeting protein oligomers as a strategy to identify new PPI inhibitors has precedence in the literature, with reports of macrocycles, peptides, and small-molecule inhibitors of IL-17A and TNF $\alpha$  that bind at the interface between oligomers and cause disruption of the signaling-competent forms of these proteins (24–27). Finally, we show that the discovery of small-molecule PPI inhibitors still often depends on serendipity, so the ability to employ multiple screens and access diverse chemical space can increase the odds for success for these challenging targets.

## Materials and Methods

**Expression and Purification of NKG2D and MICA ECDs.** The gene encoding the ECD of human NKG2D (residues 90 to 216) was synthesized with a Met-Gly at the N-terminus and Ser117Glu and Ile173Ser mutations to improve the crystallization probability of NKG2D. These mutations reside outside of the ligand binding surface and do not impact ligand binding. NKG2D was cloned into pET28a (Novagen) and expressed as inclusion bodies in *Escherichia coli* BL21(DE3) by induction with 1 mM IPTG at OD<sub>595</sub> of 1.1 to 1.4 for 3 h at 37 °C.

The cell pellet from an 18 L expression was resuspended in 600 mL of Buffer A (50 mM Tris, pH 8.0, 100 mM NaCl, 1 mM EDTA) and lysed by sonication. Inclusion bodies were collected by centrifugation at 75,000  $\times$  g and were isolated by washing twice with 20 mM Tris, pH 8.0, 100 mM NaCl, 1% Triton X-100, once with 20 mM Tris, pH 8.0, and once with 20 mM Tris, pH 8.0, 200 mM NaCl, 10 mM EDTA, and 2 mM DTT. This procedure yields 60 g of NKG2D-containing inclusion bodies.

For refolding of NKG2D, 10 g of inclusion bodies was resuspended in 100 mL of 50 mM Tris, pH 8.0, and 6 M Guanidine-HCl and stirred at 25 °C for 2 h. The insoluble material was removed by centrifugation at 75,000  $\times$  g. The supernatant was filtered, and the total protein concentration was determined by the Bradford assay. Subsequently, the filtrate was diluted dropwise into 100 mM Tris, pH 9.0, 0.5 M Arginine, 2.5 mM oxidized glutathione, 5 mM reduced glutathione, 0.1 mM PMSF at 4 °C to a protein concentration of 110  $\mu$ g/mL and incubated under gentle stirring for 72 h. This solution was concentrated and folded NKG2D was isolated by size exclusion chromatography on a Superdex75 26/60 column (Cytiva) in 20 mM Tris, pH 8.0, 50 mM NaCl. The SEC pool was further purified via Resource Q and Phenyl Sepharose to remove any trace aggregates. For crystallization, the

Phenyl pool was dialyzed into 20 mM HEPES, pH 7.0, 50 mM NaCl, and 1% glycerol, concentrated to ~5 mg/mL (as measured by UV absorption), flash-frozen in liquid nitrogen, and stored at –80 °C until use. Dimerization of the final product and complexation with MICA was confirmed by size-exclusion chromatography coupled to multi-angle light scattering.

The NKG2D ECD for the DEL screens, TR-FRET, and SPR assays was expressed by secretion from baculovirus-infected Tni insect cells for 72 h at 27 °C. This NKG2D protein construct spans residues 90 to 216 of human NKG2D and contains a gp64 secretion signal followed by a FLAG, 10-Histidine, Tobacco Etch Virus (TEV) protease site, and an Avi tag fused to the N-terminus. NKG2D from 10 L of clarified media from Tni secretion was bound to Anti-FLAG resin (Pierce), washed with 50 mM Tris, pH 8.0, 200 mM NaCl, and 10% glycerol, and eluted with a buffer containing 50 mM Tris, pH 8.5, 100 mM NaCl, 10% glycerol, and 100  $\mu$ g/mL 3X FLAG peptide (Sigma). The FLAG elution was diluted 1:1 with dH<sub>2</sub>O and further purified by ion exchange via MonoQ (Cytiva). For His-tagged NKG2D, the Q pool was polished by size exclusion chromatography on a Superdex 200 column (Cytiva) equilibrated in 20 mM HEPES, pH 7.4, 150 mM NaCl, and 10% glycerol. Biotinylated and detagged NKG2D was generated by incubation of the Q pool at 1.2 mg/mL NKG2D with 1:5 and 1:50 (w/w) of TEV protease and BirA biotin ligase, respectively, and 10 mM MgATP, 0.2 mM DTT, and 1 mM Biotin for 16 h at 4 °C. The detagged protein was collected as the flow through from a HisTRAP HP column (Cytiva) equilibrated in 50 mM Tris, pH 7.5, 200 mM NaCl, 10% glycerol, and 5 mM imidazole. This pool was polished on SEC as above. NKG2D protein stocks were concentrated to 0.9 to 1.6 mg/mL, flash-frozen in liquid nitrogen, and stored at –80 °C until use.

The ECDs of human MICA (residues 24 to 297) and ULBP1 (residues 29 to 216) were synthesized with the modified MARKS secretion signal, a FLAG-10-Histidine tag and TEV protease site at the N-terminus and an HRV3C protease site and Avi tag at the C-terminus. The coding sequence of the ECD of human ULBP6 (residues 29 to 207) was synthesized with the human growth hormone secretion signal, a FLAG-10-Histidine tag and TEV protease site at the N-terminus, and an HRV3C protease site and Avi tag at the C-terminus. The coding sequence for the ECD of human MICB (residues 24 to 297) was synthesized with the IgK secretion signal, a FLAG-10-Histidine tag and TEV protease site at the N-terminus, and an HRV3C protease site and Avi tag at the C-terminus. Each gene was cloned into the vector pcDNA3.4 for production in mammalian cells. For protein expression, HEK293 cells were transfected with the MICA expression construct according to the manufacturer's instructions in the ExpiFectamine 293 kit. Cell cultures were grown under shaking (37 °C, 130 to 140 RPM, 8% CO<sub>2</sub>, 80% humidity) in a Climo-Shaker ISF1-XC Incubating Shaker (Kühner Shaker X). After 72 h, the cells were collected by centrifugation at 1,000  $\times$  g for 15 min at 4 °C, and the clarified media was removed for purification of secreted MICA. Before purification, 5 mM imidazole and 2 Protease inhibitor tablets (Pierce) were added to the clarified media. Subsequently, the media was loaded onto 2  $\times$  5 mL HisTrapExcel columns (Cytiva), washed with 25 to 50 mM imidazole, and then eluted with a linear gradient from 50 to 400 mM imidazole. Elution fractions containing the protein ECD were pooled, concentrated, and loaded onto a Superdex 200 16/600 column (Cytiva) equilibrated in 20 mM HEPES, pH 7.4 150 mM NaCl. Each protein eluted as a single monomeric peak from the SEC column and fractions were pooled, flash-frozen in liquid nitrogen, and stored at –80 °C.

For TR-FRET assays, MICA was site-specifically labeled at a single free cysteine Cys-273. To fully reduce Cys-273 prior to labeling, 2 mM DTT was added to the protein for 1 h on ice. The DTT was removed by desalting into 50 mM Tris, pH 8.0, 150 mM NaCl on a HiPrep 16/60 G25 column (Cytiva), and the desalted protein pool was concentrated to 1.5 mg/mL. In order to provide sufficient material for the HTS, 90 mg of MICA was labeled in five separate reactions with each one containing 16 mg protein. A 5 mM solution of AF647-C5-maleimide (Life Technologies) in DMSO was added dropwise to a dye-to-protein ratio of 4:1 with occasional mixing of the reaction. Labeling reactions were incubated on ice in the dark until the degree of labeling reached 0.8. At this point, the reactions were quenched with 1 mM DTT, pooled, and concentrated for SEC as above. The clearly blue MICA peak was pooled and concentrated to 1 mg/mL prior to storage. The degree of labeling was calculated as 0.82 AF647 molecules per MICA as described in the manufacturer's instructions. MICB was labeled on Cys213 in a similar fashion.

For labeling purified ULBP1 and ULBP6 ECD protein, NHS-AF647 dye (ThermoFisher A20006) was prepared as a 5 mM stock in DMSO and shielded from light. The purified ULBP1 or ULBP6 ECDs at a concentration of 38  $\mu$ M were

incubated with 380  $\mu\text{M}$  dye for 2 h at room temperature with gentle agitation in the dark. At this point, the reaction was quenched with 10 mM Tris, pH 8.0, and the protein was concentrated for SEC as above. The blue ULBP-AF647 SEC peak fractions were pooled and concentrated to 0.8 to 1.0 mg/mL prior to storage. The degree of labeling was calculated as 1.3 and 3.5 AF647 molecules per ULBP1 and ULBP6, respectively, as described in the manufacturer's instructions.

**Cellular TR-FRET Assays.** SNAP-tag (ST) technology was used to covalently label NKG2D with Tb, the TR-FRET donor of energy. DNA encoding the ST was fused to the C terminus of full-length NKG2D with a linker in a pcDNA4/TO(+) vector that also contains Zeocin and Blasticidin resistance genes. This vector was transfected into HEK293 T cells to generate a HEK tetracycline-inducible cell line stably expressing the SNAP-tagged NKG2D receptor. DAP10 was then cloned into pcDNA3.1(+)-Hygro and a double stable cell line was created. All constructs were obtained from GenScript Biotech.

All cell culture reagents and antibiotics were purchased from Invitrogen. Cells were grown in DMEM high-glucose media with 10% FBS and 200  $\mu\text{g}/\text{mL}$  Zeocin, 5  $\mu\text{g}/\text{mL}$  blasticidin, and 50  $\mu\text{g}/\text{mL}$  hygromycin. Twenty-four hours prior to assay, media containing 1  $\mu\text{g}/\text{mL}$  doxycycline (Millipore Sigma) were added to induce expression of NKG2D. After 24 h, cells were washed once in HBSS (Corning), and then, 10 mL of 1X buffer containing terbium (Cisbio) was added to each flask to label the cell surface receptor. After a 1 h incubation, cells were washed twice in cell-labeling buffer (Cisbio) to remove excess nonbound terbium. Cells were detached using Accutase and resuspended in assay buffer (HBSS with Ca/Mg, 20 mM HEPES, and 0.1 % fatty acid-free BSA). Cells were dispensed into 1,536-well plates at a density of 1,500 cells/well in 2.5  $\mu\text{L}$ . For the primary and confirmation screens, 10  $\mu\text{M}$  test compounds were spotted using an Echo (Labcyte) as a single replicate or in triplicate for primary and confirmation screens, respectively. For the dose response, a dilution series of compounds starting from 100  $\mu\text{M}$  top concentration with an 11-point two-fold dilution were dispensed. Cells were incubated at 20  $^{\circ}\text{C}$  for 1 h prior to addition of 2.5  $\mu\text{L}$  of 60 to 300 nM MICA-Alexa647. The MICA concentration was chosen on a lot-specific basis to approximate the measured  $K_D$ . Cells were incubated for an additional h at 20  $^{\circ}\text{C}$  before reading on a Pherastar FSX (BMG Labtech) using a TR-FRET protocol (excitation 337 nm, emission 615 nm and 665 nm) with appropriate filters. For 384-well compound profiling assays, cells were plated at a density of 5,000 cells/well and the final assay volume was increased to 20  $\mu\text{L}$ .

Additional ligand displacement assays were performed using the same HEK293 T cells double-stable cells as the NKG2D/MICA assay. NKG2D expression was induced, and cells were labeled with terbium as per the NKG2D/MICA protocol. After compound addition and incubation, Alexa Fluor 647-labeled ULBP6, ULBP1, or MICB protein was added at a final concentration of 2.5 nM, 70 nM, or 700 nM, respectively (measured  $K_D$  value), and incubated for 1 h prior to measuring the 665/620 nm TR-FRET ratio.

A commercially available technical counter screen was developed using a HEK293 cell line expressing SNAP-tagged Glucagon-like-peptide 1 receptor, GLP1R, (Cisbio). Commercially available exendin 4 was conjugated to a TR-FRET-compatible fluorophore, Exendin 4-Alexa 647 (Innopep), allowing the development of a TR-FRET-based binding assay to identify compounds that are selective for NKG2D. The general assay procedure was the same as NKG2D, except that 2,000 cells/well were used.

**NKG2D SPR.** SPR measurements were performed using the Biacore 8K+ and Biacore S200 instruments (Cytiva). A StreptAvidin coated sensor chip (Cytiva) was docked and equilibrated into running buffer consisting of 1  $\times$  HBS (Cytiva), 0.005% P20 (Cytiva), and 5% (v/v) DMSO (Millipore Sigma, Burlington, MA). Next, the sensor surface was pulsed with three injections of 50 mM NaOH (Cytiva) for 60s at a flow rate of 50  $\mu\text{L}/\text{min}$ . Following chip conditioning, ECDs of human and murine NKG2D or human MICA were captured via their biotinylated Avi-tags by injecting 30  $\mu\text{g}/\text{mL}$  for 60s resulting in an immobilization level of  $\sim 4,000$  RU. Using traditional multicycle kinetics, small molecules were flowed over the NKG2D and MICA surfaces at 25  $^{\circ}\text{C}$ , 50  $\mu\text{L}/\text{min}$ , 60s association/60s dissociation, using eight-point, twofold titrations from 0.625  $\mu\text{M}$  to 80  $\mu\text{M}$ , with two preceding blank injections. Further optimization of compound concentration and association/dissociation data collection phases were carried out on a per-compound basis to achieve quality sensorgrams. For compound **3b**, while the preceding multicycle kinetic injections did not fully dissociate before the next, the  $R_{\text{max}}$  was fit locally to account for compound still bound to NKG2D. The responses at each concentration were added to estimate the total response to gain confidence in 1:1

binding for the compound size. The resulting sensorgrams were blank subtracted and solvent corrected before fitting the data to a 1:1 binding Langmuir model using Insight Evaluation Software (Cytiva).

**NKG2D Cell Killing Functional Assays.** The NKG2D cell-killing assay is a cell-based coculture assay with KHYG-1 cells (expressing endogenous NKG2D) and Ba/F3 cells (expressing the NKG2D ligand MICA and a b-gal reporter fragment; DiscoverX). Engagement between the two cell lines results in killing of the Ba/F3 cell, mediated by the NKG2D-MICA interaction. The luminescent assay signal, based on the KillingImmune-Lysis Reaction (KILR) DiscoverX technology, is proportional to the number of dead Ba/F3 cells. Briefly, KHYG-1 cells, resuspended in RPMI 1640 (Gibco) with 10 ng/mL IL-2 (Peprotech), were plated using a Multidrop Combi dispenser at 10,000 cells/well for the final volume of 3  $\mu\text{L}$  per well into white opaque 1,536-well plates (Corning, Corning). Compounds and control antibody were acoustically dispensed (Labcyte) directly into the assay plate, with the amounts dispensed dependent on the final concentrations desired. Plates were then covered and incubated 30 min at 37  $^{\circ}\text{C}$  in a 5%  $\text{CO}_2$  incubator. The Ba/F3 cells were resuspended in RPMI for a final density of  $0.33 \times 10^6$  cells/mL, and 3  $\mu\text{L}$  of the culture was dispensed using a MultiDrop Combi to all wells for a final count of 1,000 cells/well (10:1 effector:target ratio) and a volume of 6  $\mu\text{L}$ /well. The reference antibody used in this assay is the commercial anti-NKG2D monoclonal antibody, clone 1D11 (Novus Biologicals). The antibody was used at a final concentration of 20  $\mu\text{g}/\text{mL}$ . After a 6-h incubation at 37  $^{\circ}\text{C}$ , 2  $\mu\text{L}$  KILR detection reagent (DiscoverX) was added followed by a 1 h rest at room temperature prior to reading luminescence on a PHERAstar FSX plate reader (BMG Labtech). The NKG2D-mediated cell killing of Ba/F3 overexpressing all the other NKG2D ligands was also evaluated using similar coculture assays consisting of NKL cells and Ba/F3 cells lines expressing the b-gal reporter fragment and the respective NKG2DL. Briefly, compounds and control 1D11 antibody were acoustically dispensed (Echo 555) directly into the OptiPlate-384 (PerkinElmer). NKL cells, resuspended in X-VIVO 15 (Lonza) with 10 ng/mL IL-2 (Peprotech), were plated using a Multidrop Combi dispenser at 20,000 cells/well for a volume of 20  $\mu\text{L}$  per well into assay-ready plate. Plates were then covered and incubated for 30 min at 37  $^{\circ}\text{C}$  in a 5%  $\text{CO}_2$  incubator. The Ba/F3 cells were resuspended in X-VIVO 15 and dispensed using a MultiDrop Combi to all wells for a final count of 1,000 cells/well for volume of 4  $\mu\text{L}$  per well into assay plate (20:1 effector:target ratio). After a 4-h incubation at 37  $^{\circ}\text{C}$ , 8  $\mu\text{L}$  KILR detection reagent (DiscoverX) was added, and plates were incubated at RT prior to reading luminescence on a PHERAstar FSX plate reader (BMG Labtech). Note that we generated Ba/F3 cell lines expressing two common ULBP6 variants that were described to interact differently with NKG2D (7).

For PBMC killing assays, human PBMCs were isolated and cultured overnight with IL-15 at 10 ng/mL. The following day, PBMC and Ba/F3-MICA cells were combined at a 25:1 effector cell-to-target cell ratio for 4 h. The Ba/F3-MICA target cell viability was assessed by reading luminescence as described above.

**Antibody-Dependent Cell-Mediated Cytotoxicity Assay.** The ADCC KILR assay is a cell-based coculture assay with cytotoxic T lymphocytes stably expressing CD16 (V158 variant; DiscoverX) and Daudi B lymphoblast cells expressing a ProLabel-tagged housekeeping gene (DiscoverX). Opsonization of the Daudi cells with an antibody targeting CD20 (rituximab biosimilar; R&D systems) results in lysis of the Daudi cells by the CD16-expressing effector cells. The assay readout, based on the KILR DiscoverX technology, is proportional to the number of dead Daudi cells. Using this assay, small molecules that inhibit ADCC signaling pathways can be identified. For this assay, the Daudi cells are first opsonized with anti-CD20 rituximab biosimilar antibody (100 ng/mL, final concentration) for 30 min at 37  $^{\circ}\text{C}$ . Simultaneously, CD16 effector cells are treated with compounds of interest, after which the Daudi cells are added to the CD16 cell-containing wells (3 mL each at a 10:1 effector to target ratio). Daudi cells not treated with rituximab were also cocultured with effector cells as a background control. After a 4 h incubation, 2 mL of KILR detection reagent was added followed by a 1 h rest at room temperature prior to reading luminescence. As a positive control, the PI3K/mTOR inhibitor VS-5584 (Selleckchem) was used.

**Biochemical NKG2D/MICA TR-FRET Assay.** Compounds solubilized in DMSO were transferred using an Echo 555 (Labcyte) to a white 1,536-well COC plate (Corning 4570) containing 2.5  $\mu\text{L}$  of 10 nM His-NKG2D (90 to 216) in assay buffer composed of 20 mM HEPES pH 7.4 (Corning 25-060-Cl), 150 mM NaCl (VWR E529), 0.005% Polysorbate 20 (GE BR-1000-54), and 0.05% bovine serum album (Sigma

A7030) and incubated for 30 min at room temperature. Then, 2.5  $\mu$ L of 0.25 nM Anti-His-Terbium Gold (Cisbio 61HI2TL) and 200 nM Alexa Fluor 647 labeled MICA (24 to 297) was added to the plate and incubated for 60 min at room temperature. TR-FRET signal was read on a BMG Pherastar FS using 337 nm excitation and 620 nm/665 nm emission wavelengths. Data were normalized to controls and fit with four parameter Hill equation using Genedata Screener software to obtain IC<sub>50</sub>s.

**Crystallization and Structure Determination.** Frozen NKG2D (hNKG2D 90-216, S117E, I173S mutant) protein in 20 mM HEPES pH 7.0, 50 mM NaCl, and 1% glycerol buffer was thawed and concentrated to 14.3 mg/mL for crystallization trials. NKG2D protein was complexed with 2 mM compound and incubated for 1 h at 20 °C prior to crystallization. Crystals grew in 0.15 to 0.22 M NaNO<sub>3</sub>, 20 to 31% w/v PEG 3350 with microseeding in a 2:1 drop ratio of protein to reservoir solution by nanodroplet vapor diffusion. Initial crystals appeared at 20 °C after 2 d, reaching full size between 7 and 14 d. The crystals were cryoprotected with 0.15 to 0.22 M NaNO<sub>3</sub>, 20 to 31% w/v PEG 3350, 21 to 10% PEG 200 and flash-frozen in liquid N<sub>2</sub>.

Diffraction data were collected at the Advanced Photon Source Industrial Macromolecular Crystallography Association Collaborative Access Team beamline 17ID (Argonne, Chicago, IL). Reflections were processed using Xia2 and Dials (28), and the initial structure solution was obtained by molecular replacement with Phaser (29) using a single monomer of apo NKG2D from PDB code 1MPU. The structure was refined by iterative cycling between Coot (30) and Phenix (31). Restraints for the small molecules were generated by Afit (32). The occupancy of all compounds was refined as <1 because the electron density indicated the presence of two ligand orientations (one major and one minor population) related by a two-fold rotation within the induced binding pocket on the homodimer C2 symmetry axis. Crystallographic details are listed in *SI Appendix, Table S3*, and structure figures were generated with PyMOL Molecular Graphics System (Schrödinger LLC, New York). The peptide bond between Ser193–Ser194 adopted the *cis*-conformation as was first described in the Orthopoxvirus MHC Class 1-like protein bound to NKG2D (PDB 4PDC) (*SI Appendix, Fig. S9*) (33).

Quantitative analysis of the compound-induced splaying was performed by superimposing monomer B (right hand side) of all structures and then calculating the degree of rotation, rotation vector, and displacement of the center of mass of monomer A using the *Orientation, displacement, and angle measurements of helices and domains* plugin for PyMOL.

**Computational and NMR Conformational Analysis.** MacroModel and the macrocycle conformational sampling tool within MacroModel (34) from the Schrödinger suite of programs (Maestro Version 12.8.177, Release 2021-2, Schrödinger, LLC, New York) was used to generate low energy conformations of compounds **4a** and **4b**, respectively. Default parameters were employed, and the conformers were clustered by atomic RMSD to enable visualization of 50 low-energy clustered conformations (*SI Appendix, Fig. S10*).

Interproton distances derived from two-dimensional NMR EASY-ROESY experiment (35) (PMID 19065697) and J couplings from <sup>1</sup>H NMR spectra were used to fit the ensemble of conformers using StereoFitter (36) developed by MestreNova (*SI Appendix, Fig. S11 and Table S4*). All NMR spectra were recorded on a Bruker 600 MHz instrument equipped with a 5 mm BBO prodigy probe at

room temperature. A mixing time of 300 ms and a relaxation delay of 5 s were used, so quantitative distances could be determined according to NOEs  $\propto r^{-1/6}$  in DMSO. To validate whether the information obtained in DMSO was able to represent what happens under physiological conditions, a titration of PBS buffer into the DMSO solution of **4a** was carried out with incremental amounts (20 and 40%) until signs of precipitation were observed.

**Data, Materials, and Software Availability.** Atomic coordinates and density maps for NKG2D bound to compounds have been deposited at the wwPDB (<https://www.rcsb.org/>) under the following PDB IDs: **8EA5** (1a), **8EA6** (3e), **8EA7** (3g), **8EA8** (4a), **8EA9** (4d), **8EAA** (4e), **8EAB** (4f). All study data are included in the article and/or *SI Appendix*.

**ACKNOWLEDGMENTS.** We acknowledge Philochem AG for the identification of compounds **2a-2d** using their DEL platform. We thank Suzanne Akers-Rodriguez for assistance with crystallization of NKG2D complexes. Use of the IMCA-CAT beamline 17-ID (or 17-BM) at the Advanced Photon Source was supported by the companies of the Industrial Macromolecular Crystallography Association through a contract with Hauptman-Woodward Medical Research Institute. This research used resources of the Advanced Photon Source, a U.S. Department of Energy (DOE) Office of Science User Facility operated for the DOE Office of Science by Argonne National Laboratory under Contract No. DE-AC02-06CH11357.

Author affiliations: <sup>a</sup>Therapeutics Discovery, Janssen Research & Development, San Diego, CA 92121; <sup>b</sup>Therapeutics Discovery, Janssen Research & Development, Lower Gwynedd Township, PA 19002; <sup>c</sup>Discovery Immunology, Janssen Research & Development, San Diego, CA 92121; and <sup>d</sup>Discovery Immunology, Janssen Research & Development, Lower Gwynedd Township, PA 19002

Author contributions: A.A.T., M.B.H., P.-P.K., G.B., H.R.C., C.F.G., H.G., K.J.L., K.M.N., A.Y.S., N.A.V., J.W., S.B.B., J.P.E., A.G., S. Sun, J.E.T., J.D.V., H.V., M.-L.R., S. Sharma, B.T.S., and S.J.A. designed research; A.A.T., M.B.H., P.-P.K., N.K.K., J.D.B., J.C.G., D.H., H.A.P., G.B., R.B.Z., H.R.C., B.C.C., C.F.G., K.L.D.-G., H.G., A.R.H., L.L., K.M.N., E.V.P., A.Y.S., M.T., N.A.V., J.W., N.W., J.Z., M.-L.R., and S.J.A. performed research; N.K.K. contributed new reagents/analytic tools; A.A.T., M.B.H., P.-P.K., N.K.K., J.D.B., D.H., H.A.P., G.B., R.B.Z., H.R.C., B.C.C., M.C., C.F.G., K.L.D.-G., H.G., L.L., P.A.M., K.M.N., E.V.P., A.Y.S., M.T., N.A.V., J.W., N.W., J.Z., Z.S., H.V., M.-L.R., B.T.S., and S.J.A. analyzed data; and A.A.T., M.B.H., P.-P.K., G.B., K.L.D.-G., A.G., Z.S., S. Sharma, B.T.S., and S.J.A. wrote the paper.

The authors declare no competing interest.

This article is a PNAS Direct Submission.

Copyright © 2023 the Author(s). Published by PNAS. This article is distributed under Creative Commons Attribution-NonCommercial-NoDerivatives License 4.0 (CC BY-NC-ND).

<sup>1</sup>A.A.T., M.B.H., and P.-P.K. contributed equally to this work.

<sup>2</sup>Present address: External Data Acquisition, Bristol Myers Squibb, Princeton, NJ 08543.

<sup>3</sup>Present address: Target Validation and Functional Genomics, Ferring Research Institute, San Diego, CA 92121.

<sup>4</sup>Present address: Lead Discovery and Molecular Pharmacology, Trotana Therapeutics, San Diego, CA 92121.

<sup>5</sup>Present address: Department of Biology, Loxo Oncology at Lilly, San Diego, CA 92121.

<sup>6</sup>Present address: Department of Chemistry and Chemical Biology, Cornell University, Ithaca, NY 14850.

<sup>7</sup>Present address: Department of Biology, Avilar Therapeutics, Waltham, MA 02451.

1. J. Wu *et al.*, An activating immunoreceptor complex formed by NKG2D and DAP10. *Science* **285**, 730–732 (1999).
2. D. Garrity, M. E. Call, J. Feng, K. W. Wucherpfennig, The activating NKG2D receptor assembles in the membrane with two signaling dimers into a hexameric structure. *Proc. Natl. Acad. Sci. U.S.A.* **102**, 7641–7646 (2005).
3. L. L. Lanier, NKG2D receptor and its ligands in host defense. *Cancer Immunol. Res.* **3**, 575–582 (2015).
4. M. Babic, C. Romagnani, The role of natural killer group 2, member D in chronic inflammation and autoimmunity. *Front. Immunol.* **9**, 1219 (2018).
5. W. H. Shin, K. Kumazawa, K. Imai, T. Hirokawa, D. Kihara, Current challenges and opportunities in designing protein-protein interaction targeted drugs. *Adv. Appl. Bioinform. Chem.* **13**, 11–25 (2020).
6. S. J. Allen, K. J. Lumb, Protein-protein interactions: A structural view of inhibition strategies and the IL-23/IL-17 axis. *Adv. Protein Chem. Struct. Biol.* **121**, 253–303 (2020).
7. J. Zuo *et al.*, A disease-linked ULBP6 polymorphism inhibits NKG2D-mediated target cell killing by enhancing the stability of NKG2D ligand binding. *Sci. Signal* **10**, eaai8904 (2017).
8. P. Li *et al.*, Complex structure of the activating immunoreceptor NKG2D and its MHC class I-like ligand MICA. *Nat. Immunol.* **2**, 443–451 (2001).
9. S. Radaev, B. Rostro, A. G. Brooks, M. Colonna, P. D. Sun, Conformational plasticity revealed by the cocrystal structure of NKG2D and its class I MHC-like ligand ULBP3. *Immunity* **15**, 1039–1049 (2001).
10. B. J. McFarland, R. K. Strong, Thermodynamic analysis of degenerate recognition by the NKG2D immunoreceptor: Not induced fit but rigid adaptation. *Immunity* **19**, 803–812 (2003).
11. B. J. McFarland, T. Kortemme, S. F. Yu, D. Baker, R. K. Strong, Symmetry recognizing asymmetry: Analysis of the interactions between the C-type lectin-like immunoreceptor NKG2D and MHC class I-like ligands. *Structure* **11**, 411–422 (2003).
12. A. L. Hopkins, C. R. Groom, A. Alex, Ligand efficiency: A useful metric for lead selection. *Drug Discov. Today* **9**, 430–431 (2004).
13. T. E. Ryckmans *et al.*, Rapid assessment of a novel series of selective CB2 agonists using parallel synthesis protocols: A Lipophilic Efficiency (LipE) analysis. *Bio. Med. Chem. Lett.* **19**, 4406–4409 (2009).
14. P. D. S. Leeson, B. Springthorpe, The influence of drug-like concepts on decision-making in medicinal chemistry. *Nat. Rev. Drug Discov.* **6**, 881–890 (2007).
15. C. Bissantz, B. Kuhn, M. Stahl, A medicinal chemist's guide to molecular interactions. *J. Med. Chem.* **53**, 5061–5084 (2010).
16. D. L. Neri, R. A. Lerner, DNA-encoded chemical libraries: A selection system based on endowing organic compounds with amplifiable information. *Annu. Rev. Biochem.* **87**, 479–502 (2018).
17. R. K. Strong, Asymmetric ligand recognition by the activating natural killer cell receptor NKG2D, a symmetric homodimer. *Mol. Immunol.* **38**, 1029–1037 (2002).
18. S. Radaev, M. Kattah, Z. Zou, M. Colonna, P. D. Sun, Making Sense of the Diverse Ligand Recognition by NKG2D. *J. Immunol.* **169**, 6279–6285 (2002).



19. J. M. Rini, U. Schulze-Gahmen, I. A. Wilson, Structural evidence for induced fit as a mechanism for antibody-antigen recognition. *Science* **255**, 959-965 (1992).
20. E. J. Sundberg, R. A. Mariuzza, Luxury accommodations: The expanding role of structural plasticity in protein-protein interactions. *Structure* **8**, R137-R142 (2000).
21. K. C. Garcia *et al.*, Structural basis of plasticity in T cell receptor recognition of a self peptide-MHC antigen. *Science* **279**, 1166-1172 (1998).
22. J. B. Reiser *et al.*, A T cell receptor CDR3beta loop undergoes conformational changes of unprecedented magnitude upon binding to a peptide/MHC class I complex. *Immunity* **16**, 345-354 (2002).
23. M. R. Arkin *et al.*, Binding of small molecules to an adaptive protein-protein interface. *Proc. Natl. Acad. Sci. U.S.A.* **100**, 1603-1608 (2003).
24. S. Liu *et al.*, Binding site elucidation and structure guided design of macrocyclic IL-17A antagonists. *Sci. Rep.* **6**, 30859 (2016).
25. S. Liu *et al.*, Inhibiting complex IL-17A and IL-17RA interactions with a linear peptide. *Sci. Rep.* **6**, 26071 (2016).
26. M. M. He *et al.*, Small-molecule inhibition of TNF- $\alpha$ . *Science* **310**, 1022-1025 (2005).
27. J. O'Connell *et al.*, Small molecules that inhibit TNF signalling by stabilising an asymmetric form of the trimer. *Nat. Commun.* **10**, 5795 (2019).
28. G. Winter *et al.*, DIALS: Implementation and evaluation of a new integration package. *Acta Crystallogr. D Struct. Biol.* **74**, 85-97 (2018).
29. A. J. McCoy *et al.*, Phaser crystallographic software. *J. Appl. Crystallogr.* **40**, 658-674 (2007).
30. P. Emsley, B. Lohkamp, W. G. Scott, K. Cowtan, Features and development of coot. *Acta Crystallogr. D Biol. Crystallogr.* **66**, 486-501 (2010).
31. P. D. Adams *et al.*, PHENIX: A comprehensive Python-based system for macromolecular structure solution. *Acta Crystallogr. D Biol. Crystallogr.* **66**, 213-221 (2010).
32. S. Wlodek, A. G. Skillman, A. Nicholls, Automated ligand placement and refinement with a combined force field and shape potential. *Acta Crystallogr. D Biol. Crystallogr.* **62**, 741-749 (2006).
33. E. Lazear *et al.*, Structural basis of cowpox evasion of NKG2D immunosurveillance. *bioRxiv* [Preprint] (2019). <https://doi.org/10.1101/796862> (Accessed 1 July 2022).
34. D. Sindhikara *et al.*, Improving accuracy, diversity, and speed with prime macrocycle conformational sampling. *J. Chem. Inf. Model.* **57**, 1881-1894 (2017).
35. C. M. Thiele, K. Petzold, J. Schleucher, EASY ROESY: Reliable cross-peak integration in adiabatic symmetrized ROESY. *Chemistry* **15**, 585-588 (2009).
36. A. Navarro-Vazquez, R. R. Gil, K. Blinov, Computer-assisted 3D structure elucidation (CASE-3D) of natural products combining isotropic and anisotropic NMR parameters. *J. Nat. Prod.* **81**, 203-210 (2018).